Modulation of western South Atlantic marine heatwaves by meridional ocean heat transport

Marlos Goes[1,2,*], Shenfu Dong[2], Gregory R. Foltz[2], Gustavo Goni[2], Denis L. Volkov[1,2], Ilana Wainer[3]

[1]University of Miami, CIMAS, USA.

[2]NOAA AOML, USA.

[3]University of Sao Paulo, Brazil.

Corresponding author: Marlos Goes (marlos.goes@noaa.gov)

Key Points:

- Marine heat waves and Cold spells associated to westward propagating sea level anomaly features.
- Horizontal advection important for the mixed layer heat budget in the western South Atlantic.
- AMOC leads the beginning of propagating mode in the east by 3-9 months.

Abstract

Marine heatwaves and cold spells are extreme surface temperature events that have been associated with adverse societal and ecosystem impacts in several regions around the globe. Predicting these events presents a challenge because of their generally short-lived nature and dependence on air-sea interactions, both locally and remotely. Here we analyze oceanic propagating features that promote the occurrence of marine heatwaves and cold spells in the western subtropical South Atlantic. The main interannual feature detected from satellite sea level data since 1993 shows a westward propagating zonal pattern with a periodicity of 3-5 years. The pattern has a significant in-phase correlation with sea surface temperature (SST) anomalies in the western South Atlantic, explaining 77% of the daily extreme warm (90%) and cold (10%) SST anomalies and consequently modulating interannual variations in the intensity and duration of marine heatwave and cold spell events. It is found that meridional oceanic advection plays an important role in the regional heat budget associated with the westward-propagating mode, modulating the meridional exchange of tropical (warm) and extratropical (cold) waters in the western subtropical South Atlantic region and thereby setting a baseline for temperature extremes on interannual timescales. This propagating mode is well correlated ($r > 0.6$) with the strength of the meridional overturning circulation at 25°S and 30°S with a lag of approximately 5 to 9 months. The lagged response provides a potential for predictability of extreme events in the western South Atlantic.

Plain Language Summary

Here we show that ocean dynamics can affect Marine Heat Waves (MHWs) and Cold Spells (CSs) in the western subtropical South Atlantic. We focused our analysis on the sea level anomaly features that propagate westward, crossing the basin in 3-5 years near 30S. As they propagate, the sea level anomalies drive clockwise (for negative anomalies) or anticlockwise (for positive anomalies) ocean circulation around them. The circulation transports either tropical or subpolar waters into the subtropical region, warming and cooling the subtropical region, respectively, and influencing MHWs and CSs. Since the anomalies influence meridional ocean transport, we analyzed their link to the basin integrated meridional heat transport associated with the Atlantic Meridional Overturning Circulation. We show that there is a good correlation between the phase of the sea level and circulation anomaly propagation (either centered in the eastern, western or interior of the basin) and the meridional heat transport. Therefore, the AMOC index can serve as an early warning for a multi-year prediction of MHWs and CSs in the subtropical western South Atlantic.

1 Introduction

Marine heatwaves (MHW) and cold spells (CS) are sustained extreme warm and cold sea surface temperature (SST) anomalies, respectively. In particular, MHWs have received considerable attention in recent years because their persistence and intensity can have drastic impacts on marine ecosystems, such as coral bleaching (Couch et al., 2017; Dalton et al., 2020; Le Nohaïc et al., 2017), reduced primary productivity (Sen Gupta et al., 2020), pelagic species mortality (Smale et al., 2019), and closing of commercial and recreational fisheries (Cavole et al., 2016; Stuart-Smith et al., 2018). The compound effect of MHWs with other stressors such as ocean acidification, tropical cyclones, algae blooms, and marine pollution, can have long-term impacts on the marine ecosystems. In addition to these stressors, global warming affects the baseline of transient anomalies (Hobday et al., 2018) and, therefore, may increase the duration, frequency and intensity of MHWs in most regions of the globe (Frölicher & Laufkötter, 2018; Oliver et al., 2018; Costa and Rodrigues, 2021).

One of the most resilient MHW events was registered in the Northeast Pacific region during 2013-2016. This event, commonly known as the "Blob", has been linked to large scale atmospheric and oceanic patterns such as a reduction in wind-driven upper-ocean mixing and a shallow mixed layer depth (Amaya et al. 2020; Di Lorenzo and Mantua 2016; Joh and Di Lorenzo 2017). Other recent studies have shown the importance of the ocean state for similar types of extreme temperature anomalies in different basins. For instance, the occurrence, location and intensity of MHWs in the Tasman Sea have been linked to upper 2000 m warm ocean heat content anomalies on interannual to decadal timescales (Behrens et al. 2019), and the likelihood of MHWs near the East Australian Current has been shown to be modulated by westward propagation of Rossby waves (Li et al., 2022).

In the western South Atlantic, Rodrigues et al. (2019) linked the occurrence of MHWs to blocking atmospheric events associated with atmospheric Rossby wave trains propagating from the South Pacific Ocean. These blocking events are characterized by increased atmospheric sea level pressure, suppressed formation of clouds and increased solar radiation into the ocean. For some MHW events, this mechanism can be the trigger. However, the large-scale ocean circulation may precondition or interact with these events and, thus, modulate their occurrence on interannual timescales. For example, Goes et al. (2019) showed that the South Atlantic MHW during the austral summer of 2009/2010 propagated zonally from the center of the basin to the east coast of South America near 22°S. Upon reaching the western boundary, this MHW propagated southwards along the Brazil Current and dissipated two months later near 30°S. The mechanisms by which large-scale ocean processes may influence MHW events in the South Atlantic are mostly unknown. In other locations, such as the North Atlantic, the tripole pattern, which is the first mode of interannual variability of SST and sea level anomaly (SLA), has been linked to convergences and divergences of the integrated meridional heat transport, which impacts the large scale upper ocean heat content and coastal sea level in neighboring areas (e.g., Roberts et al., 2016; Volkov et al., 2019a,b).

In the South Atlantic, evidence has been found that the large scale SST pattern can serve as a fingerprint for South Atlantic Meridional Overturning Circulation (AMOC) variability (Dima and Lohman, 2010; Lopez et al., 2016), which may change the baseline for the occurrence of MHW and CS events in the region. This paper analyzes the effect of basin-scale propagating ocean anomalies on the occurrence of MHW and CS in the western South Atlantic. Known methodologies (Section 2.2) are used to detect the propagating modes and the extreme temperature events. A mixed layer heat budget analysis is presented to investigate the role of ocean advection and heat fluxes in the western South Atlantic. Finally, a reconstruction of the AMOC in the South Atlantic will be used to infer the role of large-scale volume and heat transport in triggering these anomalies. The potential to predict these events is also discussed.

2 Data and Methods

2.1 Data

Five main data sets are used in this work, consisting of SST and sea level height from remote sensing, reanalyses for the ocean (ORAS5) and air-sea interface (ERA5), and an AMOC reconstruction from satellite altimetry and in-situ temperature.

The analysis of SST data is performed using the NOAA Optimum Interpolation Sea Surface Temperature data set (OISSTv.2; Reynolds et al. 2007), a blended global gridded product available daily at a 1/4° horizontal resolution since January 1982. Daily resolution is used to identify metrics of MHW and CS, and monthly resolution is used in basin-scale correlation maps. For the purpose of this work, the SST data are spatially regridded using a bilinear interpolation to a 1° x1° horizontal resolution from 1993 to 2020.
The sea level analysis is performed using the monthly maps of sea level anomaly (SLA) from 1993 to 2020 processed and distributed by the Copernicus Marine Environment Monitoring Service (CMEMS). The SLA maps are produced on a 1/4° grid (Taburet et al., 2019) by merging data from all altimetry satellites available at a given time (Pujol et al. 2016). The SLA data at each grid point is computed with respect to a twenty-year (1993-2012) mean. The seasonal cycle is removed by subtracting the climatological monthly means computed for the whole analyzed period.
Surface atmospheric variables used in this study come from the European Centre for Medium-Range Weather Forecasts' (ECMWF) ERA5 Reanalysis (Hersbach et al., 2020). We use monthly fields of zonal and meridional wind, sea level pressure (SLP), and surface heat fluxes (shortwave, longwave, latent and sensible) from 1993 to 2020.
The monthly AMOC strength timeseries at four different latitudes in the South Atlantic (35°S, 30°S, 25°S, and 20°S) for the period 1993-2021 were produced using synthetic temperature profiles based on statistical relationships between SLA and the depths of isotherms (Dong et al., 2015, 2021), salinity profiles from historical T/S relationships (Goes et al., 2018), and monthly surface wind stress data from ERA5. The methodology has been validated against the AMOC and meridional heat transport estimates based on cross-basin expendable bathythermograph (XBT) high-density transect data near 35°S (Dong et al., 2015).
We examine vertical temperature anomalies and calculate the heat budget in the western South Atlantic using the ORAS5 reanalysis (Zuo et al., 2018), which is based on an ensemble of global eddy-permitting (0.25°) ocean model runs, forced with air-sea fluxes from ERA5 since 1979. The monthly output of ORAS5 is interpolated to a 1x1° horizontal grid and 75 vertical levels. For this work, we use the following ORAS5 fields: temperature (T), horizontal velocity ($\boldsymbol{v}$), mixed layer depth (h), wind stress (τ) and net surface heat flux ($Qnet$) from 1993 to 2021.

2.2 Methods

2.2.1 Complex EOF

To define the interannual propagating patterns of SLA in the South Atlantic, first the monthly de-seasoned SLA fields are filtered using a bandpass wavelet filter of 0.8 to 16 years. Then we perform a Complex Empirical Orthogonal function (CEOF) analysis (e.g., Navarra and Simoncini, 2010; O'Kane et al., 2014) to extract the main propagating patterns of variability between 15°S and 40°S. The CEOF uses a principal component analysis on a Hilbert transform of a field. Therefore, it produces real and imaginary parts of loadings (maps), here defined as $\boldsymbol{CEOF_j(x,y)}$ for a particular mode $\boldsymbol{j}$, and their associated expansion coefficients or principal components ($\boldsymbol{PC_j(t)}$). The CEOFs and PCs are used to compute spatial and temporal amplitudes and phases, which are necessary to describe a propagating wave pattern (Majumder et al., 2019). The SLA, associated with a particular mode of the variability $\boldsymbol{j}$ (SLA_j), can be reconstructed as the product of its loadings and its associated expansion coefficients:

$$SLAj(x, y, t) = PC_j(t) \times CEOF_j(x, y). \quad (1)$$

The time evolution of the mode $\boldsymbol{j}$ can be examined by rotating in phase the CEOF and the PC by an angle θ using a rotation matrix $R_{2x2}(\theta)$, which produces the same reconstruction:

$$SLAj(x, y, t) = R(\theta).PC_j(t) \times R(\theta).CEOF_j(x, y) \quad (2)$$

Cross-correlations and composites of SST, SLP and 10-m wind anomalies are obtained for the rotated phases of the CEOF modes. To remove sub-annual timescales, the monthly anomalies are detrended and low-pass filtered using either a 13-month or 19-month Gaussian filter as specified.

2.2.2 Marine Heatwaves and Cold Spells

Extreme SST anomaly (SSTA) events are defined as SSTA above the 90^{th} percentile for MHW and below the 10^{th} percentile for CS. The MHW and CS characterization follows the method described in Hobday et al. (2016), using detrended daily values of SSTA at a 1° x 1° degree horizontal resolution. The K-means cluster analysis (Arthur and Vassilvitskii, 2007), which is a method that minimizes the Euclidean distance between groups of observations, is used to determine the large-scale patterns associated with the SSTA during the MHW or CS event, therefore categorizing the extreme SSTA in spatial and temporal domains. In the analysis, we defined 5 clusters using the duration, maximum intensity, mean intensity and location as input parameters of MHW/CS.

2.2.3 Mixed Layer Heat budget

To examine the roles of atmospheric and oceanic contributions to the mixed layer temperature changes, we use a simplified temperature tendency equation:

$$\underbrace{\frac{\partial T}{\partial t}}_{(a)} = \underbrace{\frac{(Q_{net} - Q_{pen})}{\rho_0 C_p h}}_{(b)} - \underbrace{\boldsymbol{v} \cdot \nabla_H T}_{(c)} - \underbrace{w\frac{\Delta T}{h}}_{(d)} + \underbrace{R}_{(e)} \quad (3),$$

which states that the mixed layer temperature tendency (a) is driven by contributions from the net surface heat flux (b), horizontal advection (c), and vertical entrainment (d). The residual *R* (e) represents unresolved processes such as horizontal and vertical mixing, eddy covariances, and the accumulation of errors from the terms (a)-(d) (Vialard et al. 2001). The mixed layer depth (*h*) is calculated using the criterion of an increase in potential density of 0.03 $kg.m^{-3}$ from the surface. Mixed layer depth typically varies from 15 m to 180 m in the western South Atlantic. Temperature (T) and horizontal velocity (**v**) are averaged over the mixed layer. In (b), Q_{net} is reduced by the amount of shortwave radiation that penetrates through the base of the mixed layer (Q_{pen}), estimated from an exponential function of surface ocean color (Morel and Antonine 1994; Sweeney et al., 2005). Shortwave radiation from ERA5 is used in the Q_{pen} calculation, since ORAS5 does not provide shortwave radiation as a standard output. In addition, ocean color is derived from the SeaWiFS satellite climatological Chlorophyll-a concentration data, interpolated from its original 9 km resolution to the ORAS5 output grid. In the entrainment term (d), ΔT is the difference between the mixed layer temperature and the temperature 5 m below the mixed layer and w is the entrainment velocity at the base of the mixed layer (upward only, given by the Heaviside function: H(w>0) = 1; H(w<0) = 0), estimated as:

$$w = H(w_h + \frac{\partial h}{\partial t} + v.\nabla h), \tag{4}$$

which consists of a mass flux that crosses an isopycnal surface (Stevenson and Niiler, 1983), assuming that the Ekman pumping is the vertical advection contribution ($w_h = \nabla.\left(\frac{\tau}{\rho_0 f}\right)$), $\partial h/\partial t$ is the tendency of the mixed layer, and $\boldsymbol{v}.\nabla h$ is the horizontal induction across the mixed layer. The constants used are the density of seawater (ρ_0 = 1,025 kg m^{-3}) and the specific heat of seawater (C_p = 4000 J kg^{-1} K^{-1}).
The horizontal advection term (c) can be further decomposed into its mean (bar) and time-variable (prime) constituents:

$$uT_x + vT_y \approx \overline{u+v}\overline{T} + u'\overline{T_x} + v'\overline{T_y} + \bar{u}T_x{}' + \bar{v}T_y{}' \tag{5},$$

where the subscripts denote the gradient in the x and y directions, the mean variability is defined as a 30-year mean, and the time-variable component is the residual from the mean.

3 Results

3.1 The main propagating mode in the South Atlantic

The main propagating mode of SLA at interannual timescales in the South Atlantic (CEOF1) is an east-west pattern between 25°S and 35°S, with a periodicity of 3-5 years (Majumder et al., 2019; **Figure 1c**). This mode explains ~28% of the interannual variance of SLA in the South Atlantic. The correlation between the reconstructed SLA and the band-pass SLA reaches r = 0.75, and the correlation with SSTA reaches r=0.7, averaged over 33°S-27°S and 46°W-35°W in the western subtropical South Atlantic (**Figure 1c**). The evolution of this pattern for half-cycle (0-180° phase) snapshots every 45° (**Figure 1a**) shows that this mode has a signature in the South Atlantic SST field (**Figure 1b**), in that the correlation of SSTA with this mode shows an in-phase relationship pattern, where positive (negative) SLA are associated with high (low) SSTA. These co-located in-phase SLA and SSTA are observed mostly in the eastern and western parts of the basin. In the center of the basin, the anomalies in sea level and SST do not overlap; instead the SST correlation map shows a dipole pattern centered at ~30°S, which hints at an exchange of waters from north and south of the region. This SST dipole pattern is similar to the South Atlantic Subtropical Dipole mode (SASD), which is the leading EOF mode of interannual SST variability in the South Atlantic, explaining about 24% of the total variance (e.g., Morioka et al., 2011; Wainer et al., 2014). This mode has been linked to changes in the strength of the subtropical high, which interacts with SST by changing the wind speed pattern and latent heat flux (Sterl and Hazeleger, 2003).

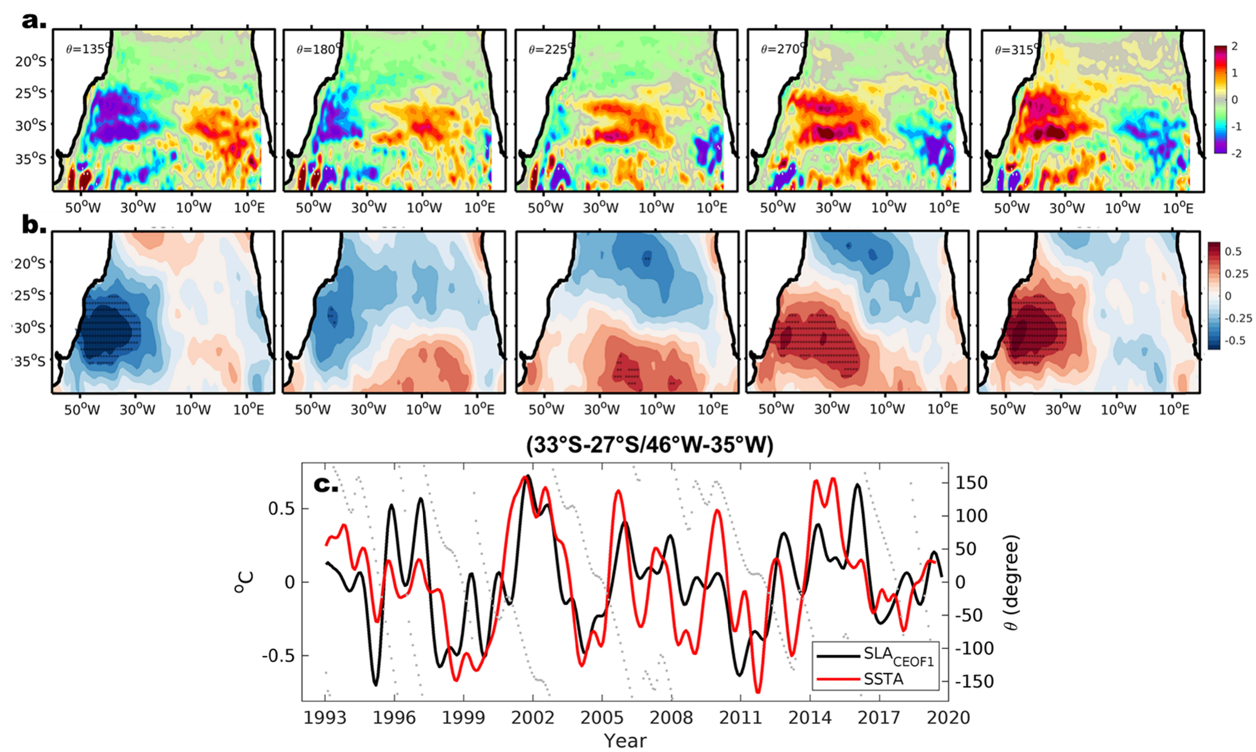

Figure 1: (a) SLA spatial phase (cm) of the first interannual CEOF mode at 45° phase snapshots. (b) Correlation of SST anomalies from 1993 to 2020 with the PC1 timeseries for the respective temporal phases shown on top. SST anomalies were previously low-passed with a 13-month Gaussian filter. Hatched regions show the statistically significant regions according to a double tailed Student t-test method. (c) Timeseries of SST anomalies (red) and SLA reconstructed by the CEOF1 (black) averaged between 33S-27S/46W-35W. Dots are the temporal phase (in degrees) from the CEOF mode.

The vertical structure of temperature anomalies and their association with propagating SLA events are shown in **Fig. 2**. The longitude-time diagram of the upper 300 m temperature anomalies (T300) from ORAS5 reanalysis and SLA (**Fig. 2a**), averaged between 32°S and 28°S, shows that T300 propagates along with the SLA from east to west in approximately 5 years. The vertical structure of these temperature anomalies in two different longitudinal areas, [15-20]°W and [35-40]°W (**Fig. 2b,c**), shows that they are generally subsurface intensified and located mostly in the upper 200 m near the base of the mixed layer. This association suggests that SST anomalies are linked to ocean dynamics and heat transport.

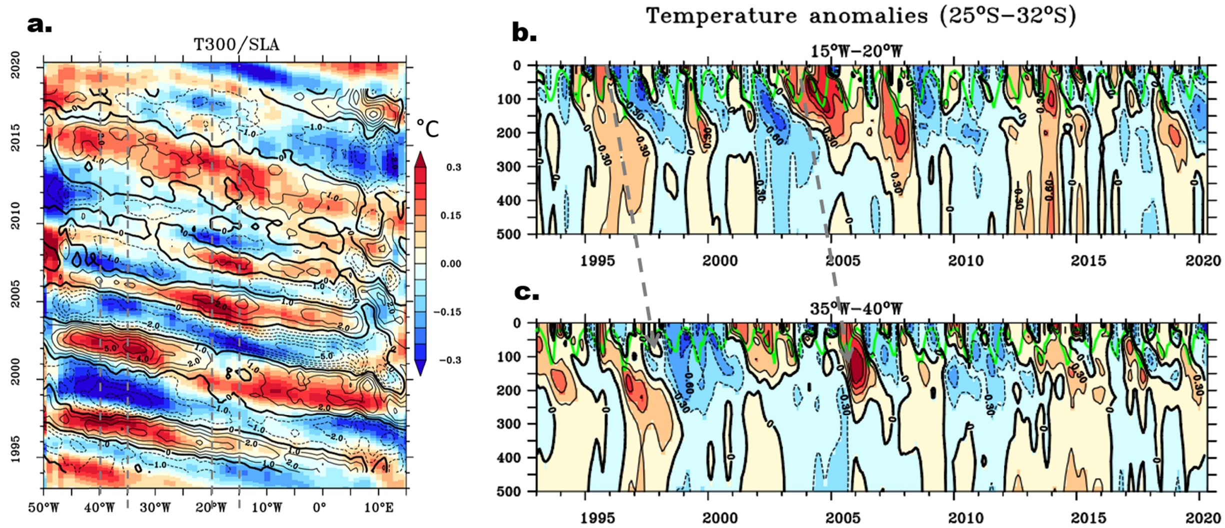

Figure 2: (a) Longitude-time evolution of the monthly temperature anomalies from ORAS5 reanalysis averaged between 28-32°S and over the upper 300 m (shaded) overlaid by monthly SLA in meters (black contours). Data was detrended, the zonal means were subtracted to show the propagating features, and a 25-month triangular filter was applied to highlight the interannual variability. Time-depth evolution of detrended ORAS5 temperature anomalies averaged between 28-32°S and between the longitudinal ranges of (b) 15-20°W, and (c) 35-40°W.

3.2 Detection of Marine Heatwaves and Cold Spells

Given the in-phase relationship found between the propagating SLA and SST signals in the South Atlantic, in this section we investigate whether this mechanism can serve as a precursor for the frequency and duration of extreme daily near-surface temperature. Applying a cluster analysis to the extreme SST events calculated on a 1°x1° grid, we define the MHW and CS modes in the western South Atlantic that show similar patterns: large-scale cooling (**Fig. 3a**) and warming (**Fig. 3b**) centered near 30°S/30°W with a maximum intensity of approximately 0.6 °C. The temporal evolution of their occurrence and intensity shows year-to-year variability with a slight trend toward more frequent MHW events in recent years relative to CS.

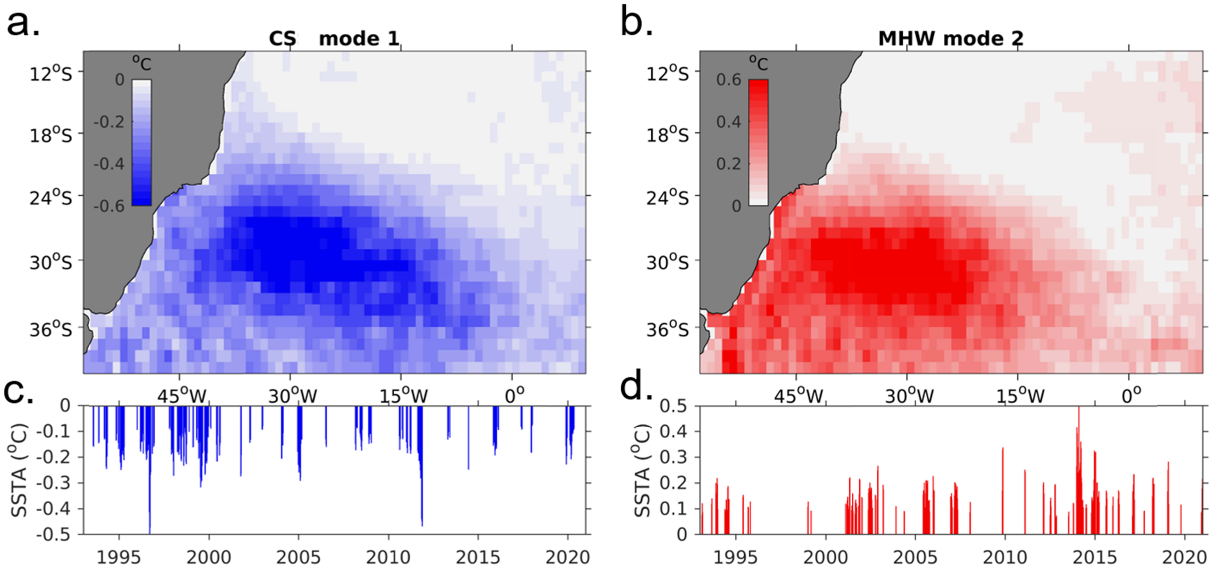

Figure 3: Marine (a,c) cold spell and (b,d) heatwave SST anomaly modes derived from a cluster analysis. Top panels (a,b) show the spatial maps of the anomalies and bottom panels (c,d) are the respective time series calculated from the averaged patterns on panels (a,b).

To understand the co-variability of the extreme SST events and the propagating SLA features, the joint variability of MHW and CS cluster modes of **Figure 3** is compared with the reconstructed SLA from the CEOF1 mode in the western South Atlantic (**Fig. 4a**). A clear correspondence between the extreme SST events and the propagating SLA mode is observed, in which daily warm SST extremes are associated with high SLA anomalies, and vice-versa. To quantify this relationship, a conditional probability is calculated. The probability of MHW and CS events conditional to the CEOF phase is calculated using the Bayes' theorem (Supplementary Material). Four probabilities are examined, which are calculated from the combination of two binary variables, one associated with the sign of the CEOF1 SLA reconstruction (CEOF+, CEOF-) and the other to the occurrence of extreme daily SST events (MHW, CS). The estimated values of conditional probabilities (**Fig S1**) suggest that the occurrence of extreme SST events and SLA with the same phase, i.e., P(MHW | CEOF+) = 69.7% and P(CS | CEOF-) = 84.2%, are much more likely than the events with opposite phase, i.e., P(MHW | CEOF-) = 15.8% and P(CS | CEOF+) = 30.3%. The total conditional probability that both MHW and CS events are in phase with the SLA reconstructed from the CEOF1 mode is calculated simply by averaging their two conditional probabilities, P(MHW | CEOF+) and P(CS | CEOF-), which results in ~ 77% of the occurrences, suggesting a strong potential for using the propagating mode to predict such extreme events.

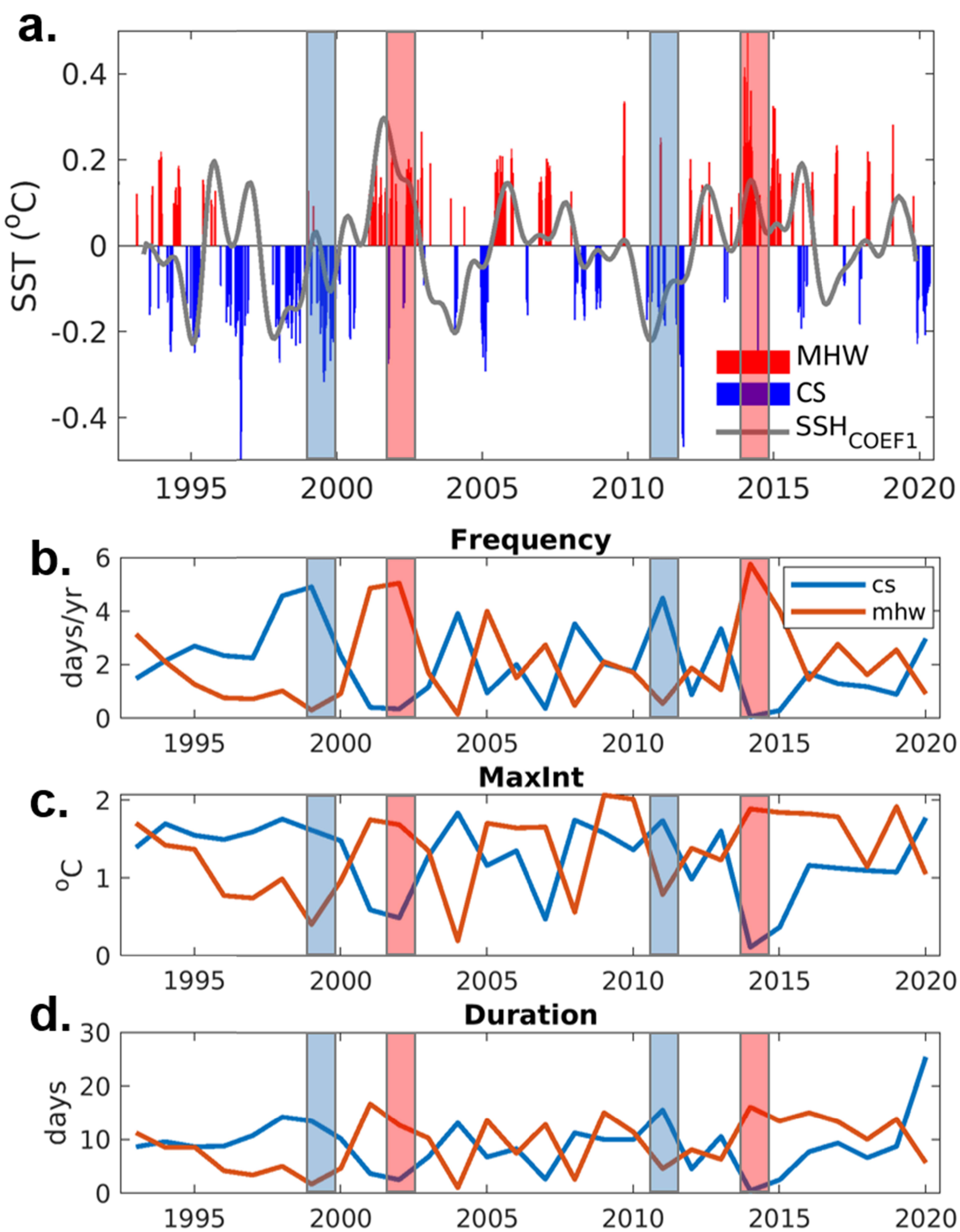

Figure 4: (a) Averaged daily SST anomalies (°C) associated to the western South Atlantic cluster mode of MHW (red bars) and CS (blue bars) overlaid by the time series of the SLA in the western South Atlantic reconstructed from the CEOF1 mode. Annual averages of (b) Frequency, (c) Maximum Intensity (MaxInt), and (d) Duration of MHW (red) and CS (blue) in the western South Atlantic.

In further analysis, the annual metrics of the MHW and CS are analyzed (**Fig. 4b, c, d)**. The time evolutions of the duration, frequency and intensity of the MHW and CS events averaged in the western South Atlantic often show out-of-phase relationships. The years with more intense, frequent and longer MHWs show weaker, less frequent and shorter CS events. Particular years that show such out-of-phase relationships are 2002/2014 for more positive (MHW) events, and 1999/2004 for more negative (CS) events. During those years with increased MHW occurrence there are approximately 5 to 6 events, with an intensity of 1.5 to 2 °C and a duration of 10 to 20 days per event. A composite analysis of the three MHW metrics for the selected years with increased and decreased MHW (**Fig. 5**) show that these events are both characterized by a dipole between the eastern and western sides of the basin. Such a pattern suggests an out-of-phase occurrence of SST extreme events between east and west, which can be related to the propagating SLA mode for those years.

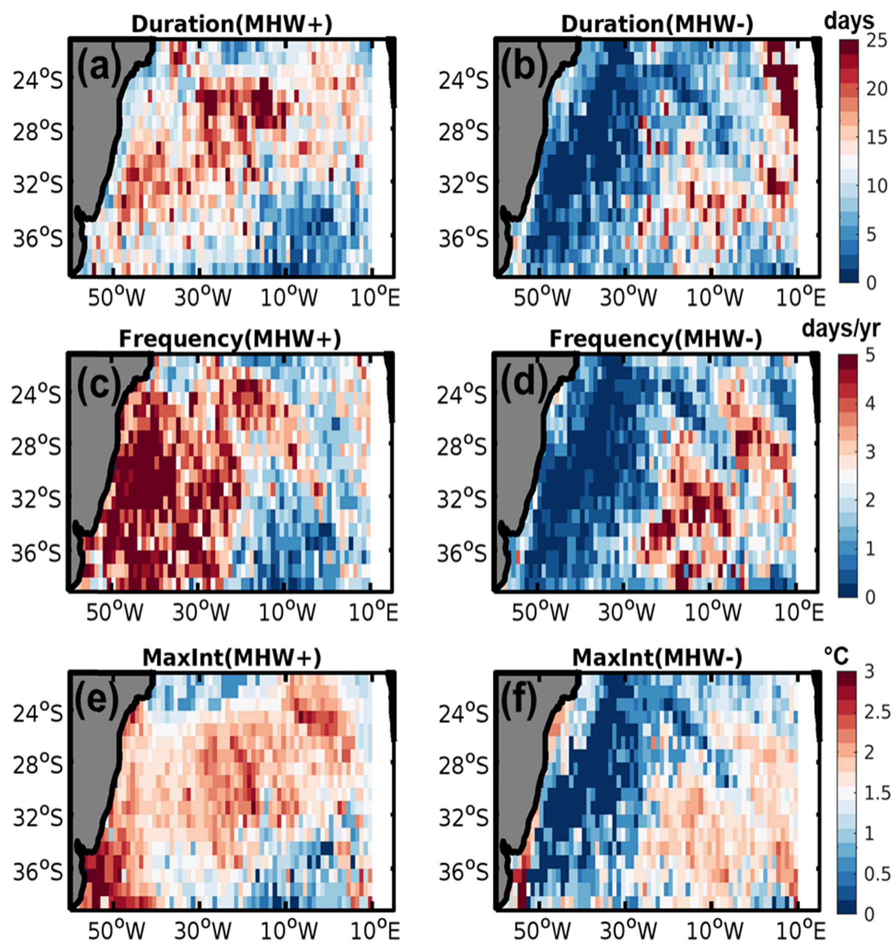

Figure 5: Composites of annual marine heatwave metrics for (left) years with high MHW occurrences (MHW+: years 2002 and 2014) and (right) for years with low MHW occurrences (MHW-: years 1999 and 2004). The MHW metrics are (a,b) duration, (c,d) frequency, and (e,f) maximum intensity (MaxInt), calculated according to Hobday et al. (2016).

3.3 Mixed Layer Heat Budget

Here, we explore the potential role of surface heat fluxes and ocean advection in modulating MHW on interannual timescales, using data from the ORAS5 and ERA5 reanalyses. The mixed layer heat budget is performed in a box within the region of maximum warming in the western

subtropical South Atlantic, defined as 35°-46°W/27°-33°S (**Fig. 6a**). The seasonal cycle of the mixed layer heat budget (**Figure S2**) is dominated by the Qnet term. Qnet warms the ocean during summer (November-March), and damps the temperature during winter (May-September). The advection term is small, and vertical advection cools the ocean during fall (March-June), a period in which the mixed layer depth increases from 20 m to 180 m. To focus on interannual timescales, monthly anomalies of the heat budget terms (equation 3) are calculated, and a low-pass filter of 19 months is applied. To understand the spatial contributions of the terms in the mixed layer heat budget, a correlation analysis was performed between ∂T/∂t and the three analyzed components (**Figure 6a-c**) by adding the components sequentially at each grid point. The correlation between ∂T/∂t and Qnet (**Figure 6a**) shows strong correlations ($r > 0.7$) particularly in the tropical region north of 25°S, and more modest correlations ($0.7 > r > 0.4$) in the subtropical region. Adding the vertical entrainment to Qnet does not increase the correlation values considerably, but some improvement is observed in the subtropical region. When horizontal advection is included, the correlations in the subtropical region north of 33°S increase almost everywhere, reaching values of r=0.9 and above, which shows the importance of the oceanic contribution to changes in mixed layer temperature in the western South Atlantic.
The time evolution of the heat budget terms averaged in the western subtropical South Atlantic (box in **Figure 6c**) estimated in ORAS5 shows that the atmospheric (Qnet) and oceanic (horizontal advection and vertical entrainment) terms contribute similarly to the SST tendency **(Fig. 6d**). The variability of the residual between the SST tendency and the sum of the atmospheric and oceanic contributions is smaller than the individual components, meaning that the residual does not have a major impact on the heat budget variability in the selected region. Other regions such as the western boundary and south of 35°S show lower correlations between changes in mixed layer temperature and the sum of atmospheric and oceanic terms (**Fig. 6c**), probably due to eddy covariance and mixing terms.
On interannual timescales, the net surface heat flux from ERA5 is mostly dominated by the latent heat flux (**Fig. 6e),** with a regression coefficient of 0.71, compared to much lower values for sensible (0.13), shortwave (0.07), and longwave (0.08) radiation components, and there is a good degree of compensation between shortwave and longwave + sensible radiative fluxes. Most of the contribution of the vertical entrainment term comes from the tendency of the mixed layer term (∂h/∂t), with smaller contributions from Ekman vertical advection and lateral induction terms (not shown). The decomposition of the horizontal advection term into meridional and zonal mean and time-variable components shows that $v'\overline{Ty}$ is by far the dominant component (**Figure 6f**). This suggests that meridional velocity is driving the oceanic exchanges in the region.

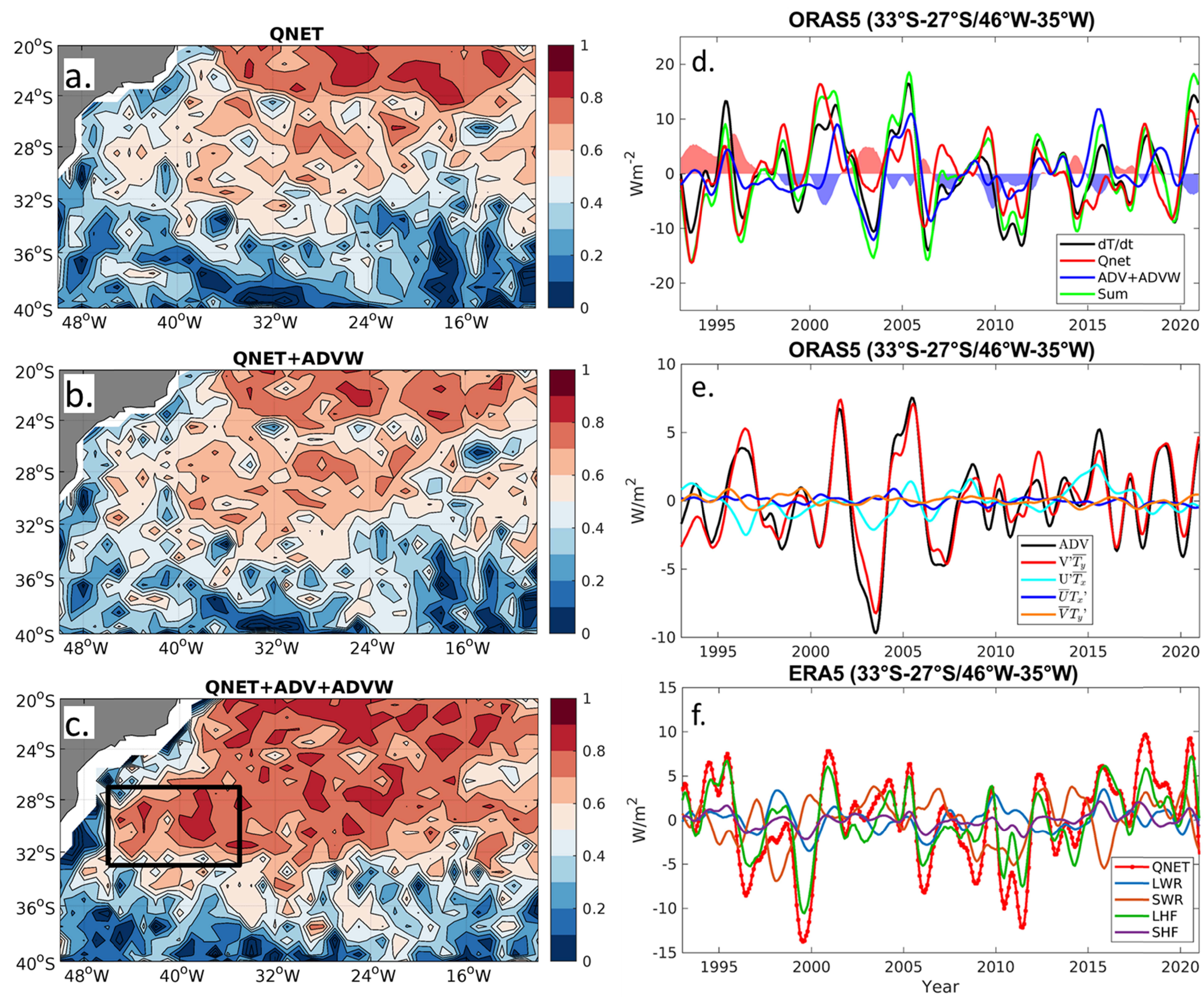

Figure 6: (a-c) Maps of correlation between the anomalies of temperature tendency (dT/dt) and the anomaly terms of the mixed heat budget: (a) Qnet, (b) Qnet + ADVW, and (c) Qnet + ADVW + ADV. The black box in (c) represents the region where the heat budget timeseries were calculated (27-33°S/35-46°W). (d) Mixed layer heat budget anomalies averaged in the box. Red/blue shading represent the residuals (dT/dt minus Sum). (f) Timeseries of the components of the anomalous surface heat flux (Qnet) from ERA5 reanalysis: latent (LHF), sensible (SHF), shortwave (SWR) and longwave (LWR) fluxes. The mixed layer budget terms are labeled mixed layer temperature tendency (dT/dt), surface fluxes (Qnet), horizontal advection (ADV), vertical advection (ADVW) and Sum = QNET + ADV + ADVW. Anomalies are calculated by subtracting the monthly climatology of the monthly averages, and Gaussian low-pass filter of 19 months is applied to the timeseries.

The results above suggest that the relationship between SLA and SST in the interior of the basin is mainly due to variations in advection and latent heat fluxes in the mixed layer (**Fig. 7**). Using the SLA field for each phase of the propagating feature, we calculated the associated geostrophic velocities from the thermal wind relationship. For better visualization, the SLA was smoothed using a 5x5 degree Gaussian filter. According to geostrophy in the Southern Hemisphere, flow is cyclonic (clockwise) around a negative SLA, and anticyclonic (counterclockwise) circulation flows around a positive SLA. Therefore, a positive SLA anomaly would favor advection of warm tropical waters ahead of the westward propagating SLA, and cooler subpolar waters behind the SLA anomaly (**Fig. 7a-d**). Warm anomalies are then generally associated with southward advection and cold anomalies with northward advection. Consequently, the dipolar SST circulation centered over the SLA monopole anomaly (**Fig. 7e, g**) is generated because of the exchange of waters between the subpolar and tropical regions that takes place in the subtropics. In addition, the CEOF1 mode is related to sea level pressure (SLP) anomalies in the center and south of the basin (**Fig. 7i-l**). SLP anomalies are collocated with SLA from the CEOF1 mode pattern at the center of the basin (90° and 270° phase angles) and have the same sign. A positive SLP anomaly (**Figure 7k**) may warm the surface locally due to a reduction of winds and cloud cover. It also generates an anticyclonic wind pattern around it, reinforcing the subtropical circulation and increasing the latent heat flux, particularly north of 30°S, thus contributing significantly to the dipole SST pattern. The opposite happens for the reverse phase (90°, **Figure 7i**). In the western side of the basin, strengthened winds may dampen the positive SSTA (**Fig. 7k,l**), similar to what was shown in Sterl and Hazeleger (2003), leading to the transition to the next phase of the oscillation.

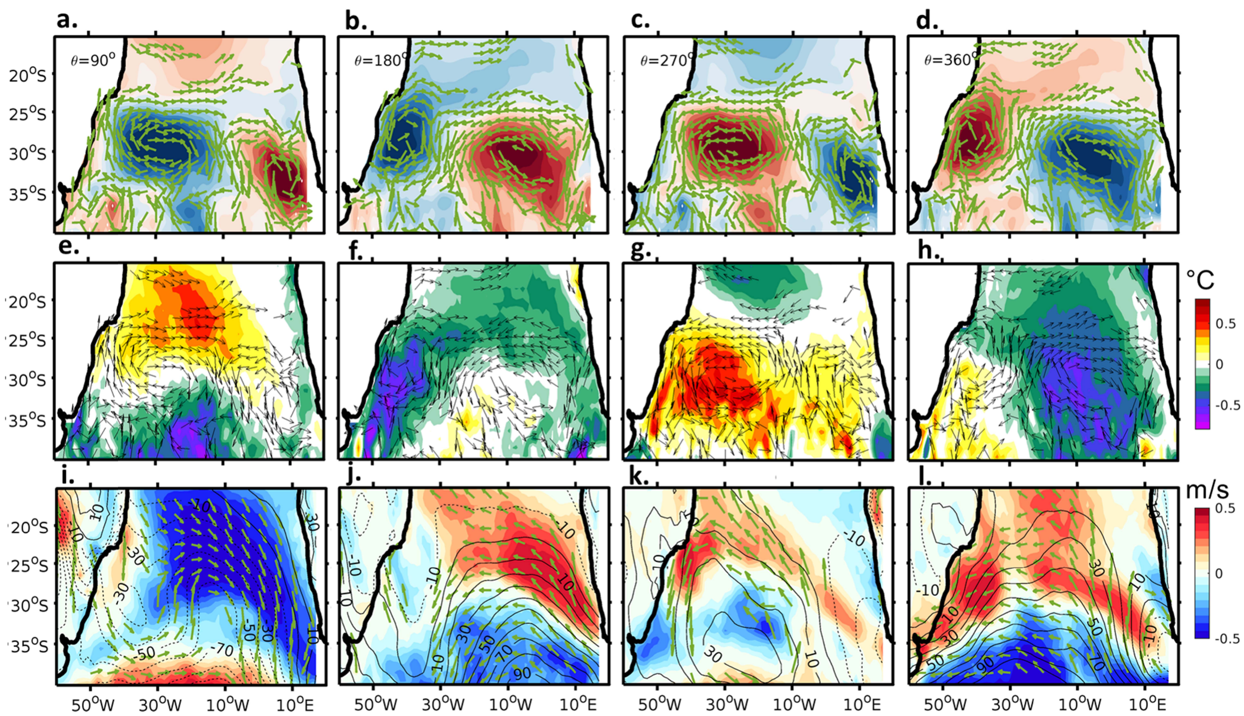

Figure 7: Composites for different phases of the propagating CEOF1 mode of SLA. Top panels: CEOF1 spatial pattern at 90° phases shown at the top left of panels a-d. The associated geostrophic current vectors are overlaid. Middle panels: Composites of SST anomalies (°C) with the geostrophic current vectors overlaid. Bottom panels: Composites of surface wind anomalies with the direction given by the arrows and speed (m/s) given by the shades. Overlaid on panels (i-l) are the contours of SLP anomalies (Pa).

3.4 Propagating SLA and AMOC

Volkov et al. (2019) showed that the tripole SLA pattern in the subtropical North Atlantic is partly driven by heat and freshwater divergence associated with the AMOC. Here, we investigate the link between the South Atlantic MOC at four different latitudes and the dominant SLA propagating feature. For this, we use the same methodology that was applied for generating **Fig. 1**, in which the CEOF1 mode is rotated in phase (**Equation 2**). Similar to a lagged correlation, we calculate the correlation between the real part of PC1 and AMOC strength for each rotation angle θ, and select the angle at which the best correlation is achieved (**Fig. 8**). This is performed with the AMOC time series at the four latitudes (20°S, 25°S, 30°S, and 34.5°S) computed by Dong et al. (2021). The AMOC time series agree reasonably well with PC1 at all analyzed latitudes, with correlations above 0.4. At 34.5°S, the phase relationship was not as clear in the beginning of the timeseries but improved after 2000. The weaker relationship may be due to the fact that the spatial pattern of the CEOF1 mode is more dominant north of 33°S. Indeed, Dong et al. (2021) showed that the AMOC at 34.5°S does not agree well with the AMOC at the other 3 latitudes further north. In addition, we can observe a slight shift toward the combination of higher angles and SLA patterns moving westward as the latitude at which the AMOC is calculated moves farther north (**Fig. 8**), suggesting that coherent anomalies are advected from the south.

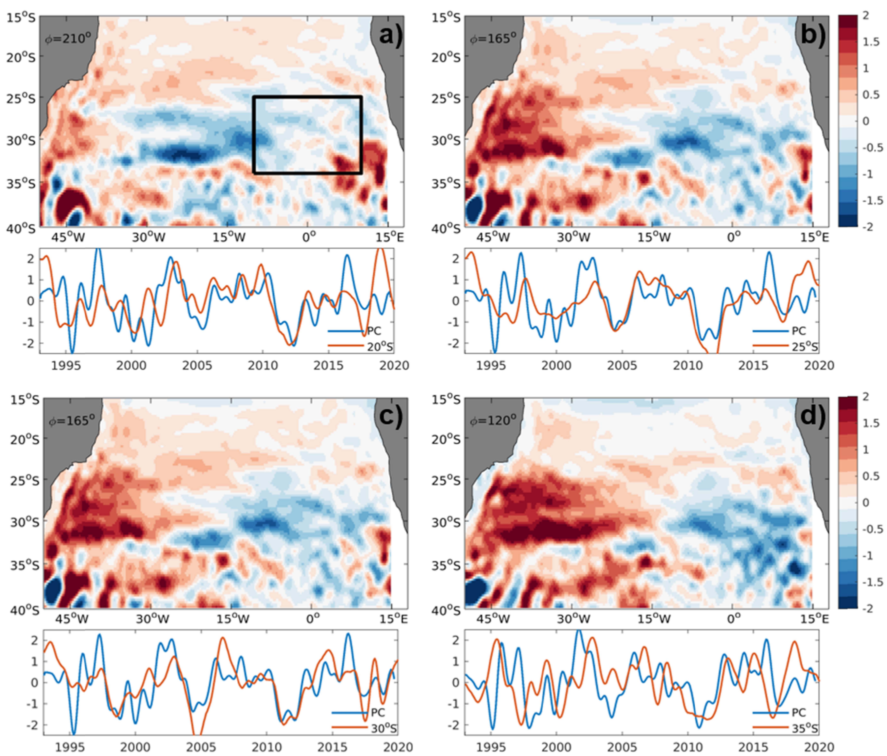

Figure 8: CEOF1 pattern of SLA in cm (maps) and PC1 (timeseries) associated with the maximum correlation between PC1 mode and the AMOC at four different latitudes: (a) 20°S, (b) 25°S, (c) 30°S, and (d) 35°S. The maximum correlation between the AMOC and the CEOF1 is estimated by rotating the CEOF1 phase. The black box in (a) shows the region where the CEOF1 reconstructed SLA is used to calculate lagged correlations with the AMOC strength (**Figure 9**).

The lagged correlation between the AMOC and SLA reconstructed from CEOF1 mode in the eastern part of the basin (25°S-33°S/10°W-10°E) (**Fig. 9**) shows that the magnitude of the correlation is largest at 30°S (r=-0.63, lag=-4; significant at 90%), followed by 25°S (r=-0.56, lag=-3), 20°S (r=-0.43, lag=-5), and 35°S (r=-0.4, lag=9). The negative correlations indicate that when the AMOC is stronger, there is a negative sea level anomaly in the east and therefore a positive SLA in the western side of the basin. These correlations are mostly driven by the geostrophic component of the AMOC, with correlations of about 0.55 for 25°S and 30°S, with the Ekman component playing a smaller role. The typical lags are between 3 and 9 months, similar to the timescales of northward propagation defined in Dong et al. (2021). The negative lags suggest that the AMOC leads the propagating pattern and therefore could be a precursor to the propagation.

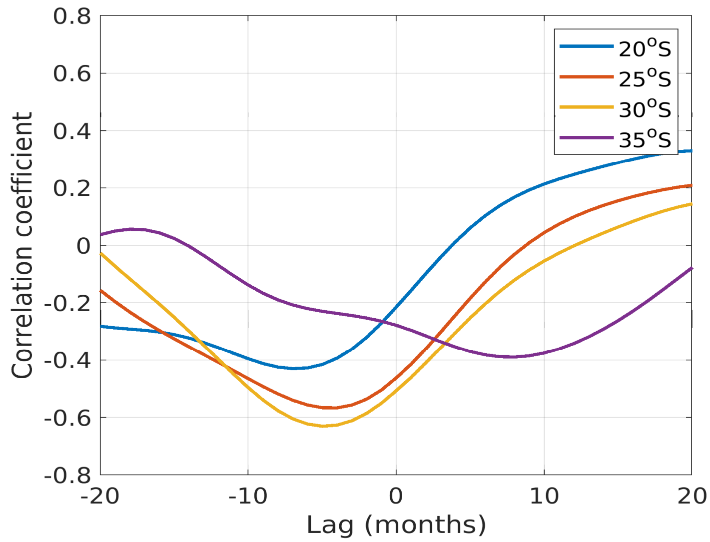

Figure 9: Lagged correlation of the reconstructed SLA in the eastern side of the basin (10°W-10°E/34°S-25°S; box in Fig. 9a) with the AMOC at four different latitudes (20°S, 25°S, 30°S and 35°S) in the South Atlantic. For negative lags, the AMOC leads SLA.

To further explore links between the propagating mode, the AMOC, and meridional heat transport (MHT), we calculated MHT across 30°S, the latitude with the highest correlation between CEOF1 and the AMOC. We divided the MHT across 30°S into western (west of 43°W), eastern (east of 3°E), and interior contributions, similar to what was performed in Dong et al. (2009) across 35°S. To focus on the upper layer of the ocean, we integrated the heat transport contributions from the surface to 500 m, instead of through the full ocean depth. The mean transport contribution in the west is southward (-0.59 +/- 0.12 PW), and it is northward in the interior (0.74 +/- 0.19 PW) and east (0.58 +/- 0.16 PW). Following the same procedure described above, the phase of the CEOF1 mode with the highest correlation with MHT anomalies is calculated for each of the three areas (**Fig. 10)**. The optimal propagation phase in each area confirms the role of the CEOF mode in regulating the amount of heat exchanged between the tropics and extratropics, as highlighted by the arrows in **Fig. 11**. As such, stronger heat transport southward in the west and northward in the interior correspond to the CEOF1 phase with a positive SLA in the west (**Fig. 10a, b**), and an increased northward transport in the east corresponds to a CEOF1 phase with high SLA in the east (**Fig. 10c**).

These results suggest that the 3-5 year propagation period of this mode from east to west could be modulated by and also modulate the AMOC on interannual timescales.

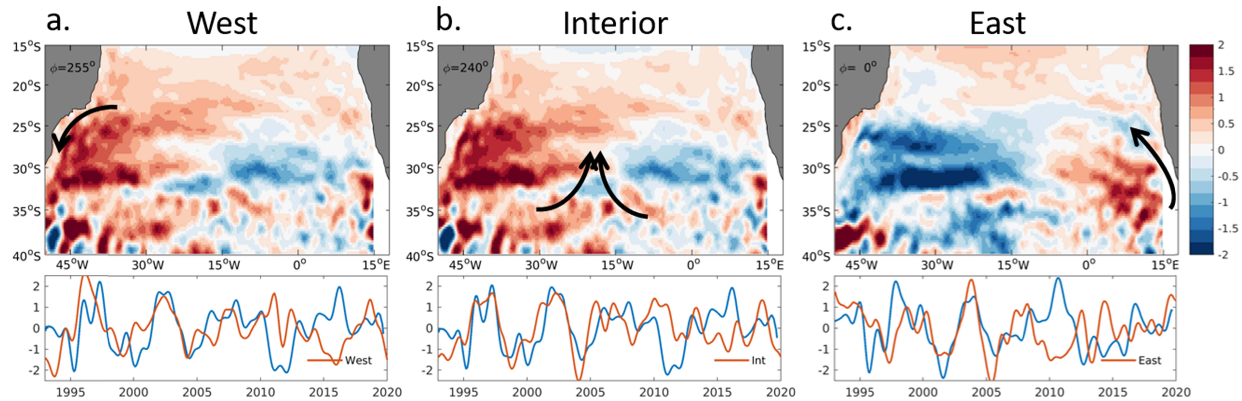

Figure 10: Same as Figure 8 but for the (a) West, (b) Interior, and (c) East components of the meridional heat transport across 30°S integrated between 0 and 500 m. The black arrows on maps show the direction of the increased geostrophic transport for each phase of the CEOF1 mode.

4 Discussion

In a recent study, Rodrigues et al. (2019) analyzed the mixed layer heat budget in the western South Atlantic for the 2014/2015 MHW event. They showed that surface heat flux anomalies, including increased shortwave radiation from reduced cloud cover and reduced latent heat loss from weaker winds, were responsible for the onset of marine heatwaves in the region. The onset of the 2014/2015 MHW was associated with the Madden-Julian oscillation (MJO) (Barreiro et al., 2019), which is the dominant mode of atmospheric variability on intraseasonal timescales in the tropics (mainly between 40-60 days; Madden and Julian, 1972). As the MJO propagates from the tropics, it affects convection, tropospheric winds, rainfall and surface fluxes (e.g., Matthews et al., 2004). On interannual timescales, El Nino Southern Oscillation (ENSO) and the Southern Annular Mode (SAM) can influence the strength and location of the South Atlantic subtropical high (e.g., Sun et al., 2018), which is also associated with the propagating mode here identified through wind stress curl or enhanced coastal upwelling in the Benguela Current System region.

The role of the ocean has received much less attention than atmospheric teleconnections. Here we show that the large-scale ocean circulation (through the AMOC) is a pacemaker for the interannual occurrence of marine heatwaves in the western subtropical South Atlantic. This relationship was hypothesized here from the strong relationship between western South Atlantic temperature anomalies and sea surface height anomalies on interannual timescales. The SLA variability in the western South Atlantic is highly correlated (r=0.77) with the main propagating mode of SLA. The propagation of this mode agrees with the first baroclinic Rossby wave mode (Majumder et al., 2019), which is linked to the large-scale ocean adjustment. This mechanism seems to be related to the one described in Colin de Verdière and Huck (1999) and Te Raa and Dijkstra (2002), in which by crossing the South Atlantic, a warm anomaly induces southward velocity perturbations to the west and northward to the east of the center of the anomaly. This leads to a phase difference between the temperature and velocity anomalies. The perturbed velocities advect warm water southward to the west and cold water northward to the east of the initial anomaly, thereby moving the warm anomaly westward. Our results suggest that, as the mode propagates, it influences the meridional heat transport of eastern and western boundary currents and the ocean interior in different phases (**Fig. 10**). A similar mechanism was also suggested for other western boundary currents (Elzahaby et al., 2021; Zhang et al., 2021). Because the AMOC consists of both boundary flows and ocean adjustment, this mechanism may modulate but also be influenced by AMOC variability. This relationship is supported by the significant correlation between the AMOC and the cross-basin SSH (**Fig. 10**). Therefore, this work highlights the importance of sustained AMOC monitoring for regional climate in the South Atlantic. The AMOC in the South Atlantic has been monitored for more than a decade by in-situ observations (e.g., Dong et al., 2009; Meinen et al., 2013), and for almost three decades using satellite observations (e.g., Dong et al., 2015, Schmid and Majumder, 2016). Previous studies have linked the AMOC to SST fingerprints in the South Atlantic (Dima and Lohman, 2010; Lopez et al., 2016), which can extend these time series back more than a century. Recently, Bodnariuk et al. (2021) found a link between the propagating modes in the South Atlantic and Indian and South Pacific basins, suggesting that there could be coherence of oceanic features throughout the Southern Hemisphere. Further investigations of links between the propagating SSH modes, the AMOC, and atmospheric teleconnections should be performed using numerical and simplified model studies.

5 Conclusions

The leading mode of the interannual variability of SLA in the South Atlantic is characterized by westward propagating anomalies centered at 30°S, with a periodicity of 3 to 5 years. The propagating SLA signals associated with this mode are positively correlated with SSTA in the western subtropical South Atlantic. The temporal phase of the propagating mode is well correlated with interannual modulations of the MHW and CS mode centered in the western South Atlantic. We estimated that there is a 77% probability that the extreme daily sea surface temperature events occur when the SLA associated with the propagating mode bears the same sign. Our analysis shows that SST modulation by SLA in the subtropical region is driven mainly by latent heat flux anomalies and by oceanic horizontal advection. The latent heat flux appears to be related to wind speed anomalies associated with the subtropical high and atmospheric waves. The oceanic advection term mediates the exchange of tropical (warm) and subpolar (cold) waters in the region **(Figure 11**): clockwise circulation around a negative SLA anomaly favors advection of cold subpolar waters toward the subtropics, while counterclockwise circulation is generated around a positive SLA anomaly. The analyzed westward-propagating mode is significantly (at 90%) correlated ($r = 0.63$) with the AMOC at 30°S, and its origin in the eastern part of the basin lags the AMOC by approximately 3 to 9 months. Therefore, the sustained AMOC observations in the South Atlantic can provide strong multi-year predictability for extreme temperature and rainfall events in the western side of the basin.

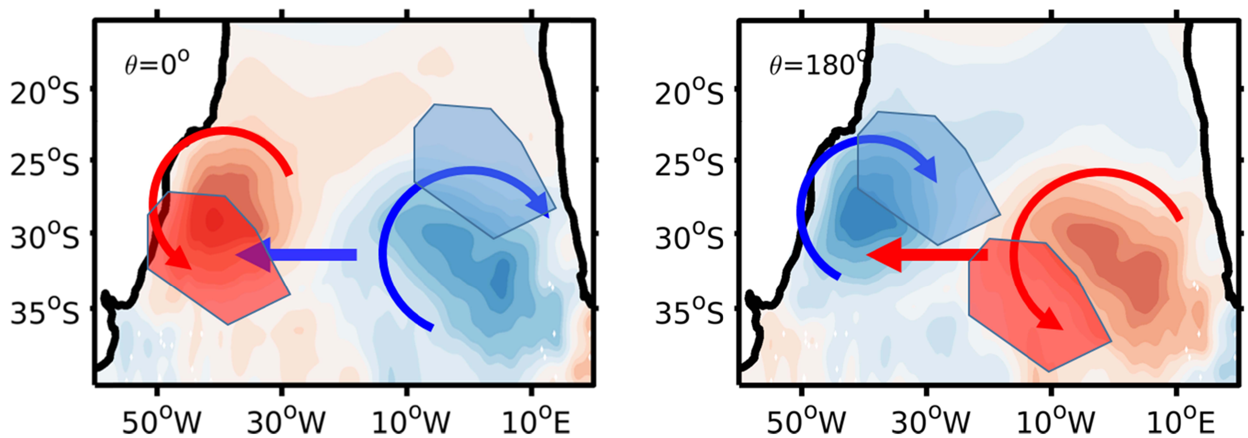

Figure 11: Schematic of the effect of the propagating oceanic heat transport on the warming and cooling of the western and eastern South Atlantic regions at two opposite phases. The contours (colored shading) are for SLA and horizontal arrows indicate westward propagation that causes cooling (left plot) and warming (right plot). The red and blue arrows indicate the tendency for warming and cooling of the regions represented by the polygonal regions.

Acknowledgments

This research was carried out under the auspices of the Cooperative Institute for Marine and Atmospheric Studies, a cooperative institute of the University of Miami and NOAA (cooperative agreement number NA20OAR4320472). MG and DLV were supported in part by the National Oceanic and Atmospheric Administration (NOAA) Climate Variability and Predictability program (grant number NA20OAR4310407) and by the NOAA Atlantic Oceanographic and Meteorological Laboratory. The authors thank S-K Lee for comments and suggestions. The Ssalto/Duacs altimeter SLA data was produced and distributed by the Copernicus Marine and Environment Monitoring Service (CMEMS) (http://.marine.copernicus.eu). The SST data comes from the https://psl.noaa.gov/data/gridded/data.noaa.oisst.v2.highres.html. ERA5 reanalysis was downloaded from https://cds.climate.copernicus.eu. The ORAS5 reanalysis was downloaded from https://www.ecmwf.int/en/research/climate-reanalysis/ocean-reanalysis. SeaWiFS Chl-a

data are available at https://oceandata.sci.gsfc.nasa.gov/SeaWiFS/Mapped/Monthly_Climatology/9km/chlor_a/.

Open Research

All calculations and figures were performed in Matlab v. 2019 and Ferret v. 7.6. The CEOF methodology was performed using the pcatool toolbox in Matlab, and the mixed layer heat budget was performed using Ferret.

References

Amaya, D. J., A. J. Miller, S. P. Xie, and Y. Kusaka (2020), Physical drivers of the summer 2019 North Pacific marine heatwave. *Nat. Commun. 11*, 1903, https://doi.org/10.1038/s41467-020-15820-w.

Arthur, D., and S. Vassilvitskii (2007), "K-means++: The Advantages of Careful Seeding." SODA '07: Proceedings of the Eighteenth Annual ACM-SIAM Symposium on Discrete Algorithms, pp. 1027–1035. (https://theory.stanford.edu/~sergei/papers/kMeansPP-soda.pdf)

Barreiro, M. et al., 2019: Modelling the role of Atlantic air–sea interaction in the impact of Madden–Julian Oscillation on South American climate. Int. J. Climatol. 39, 1104–1116.

Behrens, E., D. Fernandez, and P. Sutton (2019), Meridional Oceanic Heat Transport Influences Marine Heatwaves in the Tasman Sea on Interannual to Decadal Timescales. Front. Mar. Sci. 6, 228, https://doi.org/10.3389/fmars.2019.00228.

Bodnariuk, N., Simionato, C. G., Saraceno, M., Osman, M., & Diaz, L. B. (2021). Interannual variability of the latitude of separation of the Brazil Current: Teleconnections and oceanic Rossby waves propagation. Journal of Geophysical Research: Oceans, 126, e2021JC017557. https://doi.org/10.1029/2021JC017557

Cavole, L. M., Demko, A. M., Diner, R. E., Giddings, A., Koester, I., Pagniello, C. M. L. S., et al. (2016). Biological impacts of the 2013–2015 warm-water anomaly in the Northeast

Pacific: winners, losers, and the future. Oceanography 29, 273–285. doi: 10.5670/oceanog.2016.32

Colin de Verdière, A., and T. Huck (1999), Baroclinic instability: An oceanic wavemaker for interdecadal variability. J. Phys. Oceanogr, 29 , 893–910.

Costa, N. V., & Rodrigues, R. R. (2021). Future summer marine heatwaves in the western South Atlantic. Geophys. Res. Lett., 48, e2021GL094509. https://doi.org/10.1029/2021GL094509

Couch, C. S., Burns, J. H., Liu, G., Steward, K., Gutlay, T. N., Kenyon, J., et al. (2017). Mass coral bleaching due to unprecedented marine heatwave in Papahānaumokuākea Marine National Monument (Northwestern Hawaiian Islands). PLoS One, 12(9), e0185121. https://doi.org/10.1371/journal.pone.0185121

Dalton, S. J., Carroll, A. G., Sampayo, E., Roff, G., Harrison, P. L., Entwistle, K., et al. (2020). Successive marine heatwaves cause disproportionate coral bleaching during a fast phase transition from El Niño to La Niña. The Science of the Total Environment, 715, 136951. https://doi.org/10.1016/j.scitotenv.2020.136951.

Di Lorenzo, E., & Mantua, N. (2016). Multi-year persistence of the 2014/15 North Pacific marine heatwave. Nature Climate Change, 6(11), 1042–1047. https://doi.org/10.1038/nclimate3082

Dima, M., & Lohmann, G. (2010). Evidence for Two Distinct Modes of Large-Scale Ocean Circulation Changes over the Last Century, Journal of Climate, 23(1), 5-16.

Dong, S., S. L. Garzoli, M. O. Baringer, C. S. Meinen, and G. J. Goni (2009), Interannual variations in the Atlantic Meridional Overturning Circulation and its relationship with the net northward heat transport in the South Atlantic, Geophys. Res. Lett., 36, L20606, doi:10.1029/2009GL039356

Dong, S., Goni, G., & Bringas, F. (2015), Temporal variability of the South Atlantic meridional overturning circulation between 20°S and 35°S. Geophys. Res. Lett. 42, 7655–7662. doi:10.1002/2015GL065603.

Dong, S., Goni, G., Domingues, R., Bringas, F., Goes, M., Christophersen, J., & Baringer, M. (2021). Synergy of in situ and satellite ocean observations in determining meridional heat transport in the Atlantic Ocean. Journal of Geophysical Research: Oceans, 126, e2020JC017073. https://doi.org/10.1029/2020JC017073.

Elzahaby, Y., A. Schaeffer, M. Roughan, and S. Delaux (2021). Oceanic Circulation Drives the Deepest and Longest Marine Heatwaves in the East Australian Current System. Geophys. Res. Lett., 48 (17), e2021GL094 785, https://doi.org/10.1029/2021GL094785.

Frölicher & Laufkötter, 2018; Frölicher, T. L., & Laufkötter, C. (2018). Emerging risks from marine heat waves. Nature Communications, 9(1), 1–4. https://doi.org/10.1038/s41467-018-03163-6

Hobday, A. J. et al. (2016). A hierarchical approach to defining marine heatwaves. Prog. Oceanogr. 141, 227–238.

Hobday, A. et al. (2018).Categorizing and naming marine heatwaves. Oceanography 31.

Goes, M., J. Christophersen, S. Dong, G. Goni, and M. Baringer (2018). An updated estimate of salinity for the Atlantic Ocean sector using temperature-salinity relationships. Journal of Oceanic and Atmospheric Technology, 35(9):1771-1784, https://doi:10.1175/JTECH-D-18-0029.1.

Goes, M., Cirano, M., Mata, M. M., & Majumder, S. (2019). Long-term monitoring of the Brazil Current transport at 22°S from XBT and altimetry data: seasonal, interannual, and extreme variability. Journal of Geophysical Research: Oceans. https://doi.org/10.1029/2018JC014809

Hersbach, H, Bell, B, Berrisford, P, et al. (2020). The ERA5 global reanalysis. Q J R Meteorol Soc., 146: 1999– 2049. doi.org/10.1002/qj.3803.

Joh, Y., & Di Lorenzo, E. (2017). Increasing coupling between NPGO and PDO leads to prolonged marine heatwaves in the Northeast Pacific. *Geophysical Research Letters*, 44, 11,663– 11,671. https://doi.org/10.1002/2017GL075930

Le Nohaïc, M., Ross, C. L., Cornwall, C. E., Comeau, S., Lowe, R., McCulloch, M. T., & Schoepf, V. (2017). Marine heatwave causes unprecedented regional mass bleaching of thermally resistant corals in Northwestern Australia. Scientific Reports, 7(1), 1–11. https://doi.org/10.1038/s41598-017-14794-y

Li, Z., N. J. Holbrook, X. Zhang, E. C. J. Oliver, and E. A. Cougnon (2020). Remote Forcing of Tasman Sea Marine Heatwaves. J. Clim., 33 (12), 5337–5354, https://doi.org/10.1175/JCLI-D-19-0641.1.

Madden, R.A. and Julian, P.R. (1972) Description of Global-Scale Circulation Cells in the Tropics with a 40-50 Day Period. Journal of the Atmospheric Sciences, 29, 1109-1123. http://dx.doi.org/10.1175/1520-0469(1972)029<1109:DOGSCC>2.0.CO;

Majumder, S., Goes, M., Polito, P. S., Lumpkin, R., Schmid, C., & Lopez, H. (2019). Propagating modes of variability and their impact on the western boundary current in the South Atlantic. Journal of Geophysical Research: Oceans, 124, 3168– 3185. https://doi.org/10.1029/2018JC014812

Matthews, A.J., B.J. Hoskins, M. Masutani (2004). The global response to tropical heating in the Madden–Julian oscillation during the northern winter. Q. J. R. Meteorolog. Soc., 130 (2004), pp. 1991-2011

Morel, A. & Antoine, D. (1994). Heating rate within the upper ocean in relation to its bio-optical state. J. Phys. Oceanogr. 24, 1652–1665.

Morioka, Y., Tozuka, T. & Yamagata, T. (2011). On the growth and decay of the Subtropical Dipole mode in the South Atlantic. J. Climate 24, 5538–5554.

Morioka, Y.,T. Doi, A. Storto, et al. (2018). Role of subsurface ocean in decadal climate predictability over the South Atlantic. Sci Rep 8, 8523. https://doi.org/10.1038/s41598-018-26899-z

Oliver, E. C., and Coauthors (2018). Longer and more frequent marine heatwaves over the past century. Nat. Commun., 9, 1324, https://doi.org/h10.1038/s41467-018-03732-9.

Pujol, M.-I., Faugère, Y., Taburet, G., Dupuy, S., Pelloquin, C., Ablain, M., and Picot, N. (2016). DUACS DT2014: the new multi-mission altimeter data set reprocessed over 20 years, Ocean Sci., 12, 1067–1090, https://doi.org/10.5194/os-12-1067-2016.

Reynolds, R. W., Smith, T. M., Liu, C., Chelton, D. B., Casey, K. S., & Schlax, M. G. (2007). Daily High-Resolution-Blended Analyses for Sea Surface Temperature, Journal of Climate, 20(22), 5473-5496

Roberts, C. D., Calvert, D., Dunstone, N., Hermanson, L., Palmer, M. D., & Smith, D. (2016). On the Drivers and Predictability of Seasonal-to-Interannual Variations in Regional Sea Level, *Journal of Climate*, *29*(21), 7565-7585.

Rodrigues, R. R., Taschetto, A. S., Gupta, A. S. & Foltz, G. R. (2019). Common cause for severe droughts in South America and marine heatwaves in the South Atlantic. Nat. Geosci. 12, 620.

Roemmich, D., G.C. Johnson, S. Riser, R. Davis, J. Gilson, W.B. Owens, S.L. Garzoli, C. Schmid, and M. Ignaszewski. (2009). The Argo Program: Observing the global ocean with profiling floats. Oceanography 22(2):34–43, https://doi.org/10.5670/oceanog.2009.36.

Sen Gupta, A., Thomsen, M., Benthuysen, J. A., Hobday, A. J., Oliver, E., Alexander, L. V., et al. (2020). Drivers and impacts of the most extreme marine heatwave events. Scientific Reports, 10(1), 1–15. https://doi.org/10.1038/s41598-020-75445-3

Smale, D. A., Wernberg, T., Oliver, E. C. J., Thomsen, M., Harvey, B. P., Straub, S. C., et al. (2019). Marine heatwaves threaten global biodiversity and the provision of ecosystem services. Nature Climate Change, 9(4), 306–312. https://doi.org/10.1038/s41558-019-0412-1

Sterl, A., and W. Hazeleger (2003), Coupled variability and air-sea interaction in the South Atlantic Ocean, Clim. Dyn., 21, 559–571, doi:10.1007/s00382-003-0348-y.

Stuart-Smith, R. D., Brown, C. J., Ceccarelli, D. M., and Edgar, G. J. (2018). Ecosystem restructuring along the Great Barrier Reef following mass coral bleaching. Nature 560, 92–96. doi: 10.1038/s41586-018-0359-9

Sun, X., E. K. Vizy, K. H. Cook (2018). Land–atmosphere–ocean interactions in the southeastern Atlantic: interannual variability. Clim. Dyn., https://doi.org/10.1007/s00382-018-4155-x

Sweeney, C. et al. (2005). Impacts of shortwave penetration depth on large-scale ocean circulation and heat transport. J. Phys. Oceanogr. 35, 1103–1119.

te Raa, L. A., & Dijkstra, H. A. (2002). Instability of the Thermohaline Ocean Circulation on Interdecadal Timescales, Journal of Physical Oceanography, 32(1), 138-160.

Vialard, J., Menkes, C., Boulanger, J., Delecluse, P., Guilyardi, E., McPhaden, M. J., & Madec, G. (2001). A Model Study of Oceanic Mechanisms Affecting Equatorial Pacific Sea Surface Temperature during the 1997–98 El Niño, Journal of Physical Oceanography, 31(7), 1649-1675.

Volkov, D. L., Lee, S.-K., Domingues, R., Zhang, H., and Goes, M. (2019): Interannual sea level variability along the southeastern seaboard of the United States in relation to the gyre-scale heat divergence in the North Atlantic. Geophysical Research Letters, 46, 7481-7490, doi:10.1029/2019GL083596.

Wainer, I., Prado, L. F., Khodri, M., & Otto-Bliesner, B. (2014). Reconstruction of the South Atlantic Subtropical Dipole index for the past 12,000 years from surface temperature proxy. Scientific reports, 4(1), 1-8.

Zhang, Y., Du, Y., Feng, M., & Hu, S. (2021). Long-lasting marine heatwaves investigated by ocean planetary waves in the tropical Indian Ocean during 2015–2016 and 2019–2020. Geophysical Research Letters, 48, e2021GL095350.

Zuo, H., Balmaseda, M. A., Tietsche, S., Mogensen, K., and Mayer, M., (2019) The ECMWF operational ensemble reanalysis-analysis system for ocean and sea-ice: a description of the system and assessment, Ocean Sci. Discuss. 15, 779-808. https://doi.org/10.5194/os-15-779-2019